Applied Surface Science 593 (2022) 153450

Contents lists available at ScienceDirect

Applied Surface Science

journal homepage: www.elsevier.com/locate/apsusc

Full Length Article

Electric metal contacts to monolayer blue phosphorus: electronic and chemical properties

Pengfei Ou [a,b,*], Guoqiang Lan [a], Yiqing Chen [a], Xiao-Yan Li [b], Xiao Zhou [a,c], Cheng Chen [a,d], Fanchao Meng [e], Jun Song [a,*]

[a] Department of Mining and Materials Engineering, McGill University, Montreal, QC H3A 0C5, Canada
[b] Department of Electrical and Computer Engineering, University of Toronto, Toronto, Ontario M5S 1A4, Canada
[c] Institute of Mechanical Engineering, École Polytechnique Fédérale de Lausanne, Lausanne, Vaud CH-1015, Switzerland
[d] School of Aeronautics, Northwestern Polytechnical University, Xi'an, Shaanxi 710072, People's Republic of China
[e] Institute for Advanced Studies in Precision Materials, Yantai University, Yantai, Shandong 264005, People's Republic of China

ARTICLE INFO

Keywords:
Blue phosphorus
Schottky contacts
Fermi level pinning
Density functional theory

ABSTRACT

The contact nature when monolayer blue phosphorus (blueP) interfaces with three transition metal electrodes (i.e., Pd, Ir, and Pt) was unraveled by the *ab initio* density functional theory calculations. Specifically, n-type Schottky contact is observed for Ir(1 1 1)-blueP, in contrast, p-type Schottky contacts are formed for Pd(1 1 1)- and Pt(1 1 1)-blueP. The Fermi level is pinned partially at metal-blueP interfaces due to two interfacial behaviors: one being the modification of metal work function caused by interface dipole formation ascribed to a redistribution of charges, and the other being the production of gap states that are dominated by P *p*-orbitals since the intralayer P—P bonds are weakened by the interfacial metal-P interactions. The incorporation of metal substrates would also significantly alter the chemical properties of the adsorbed monolayer blueP. The binding strength of hydrogen can be enhanced by as much as 0.9 eV, which resulted from two parts: one is the charge transfer from metal substrate to monolayer blueP rendering a stronger H—P coupling; the other is a strong interfacial interaction after the hydrogen adsorption. The free energy change of H adsorption onto Ir(1 1 1)-blueP is as low as 0.16 eV which is comparable to the most efficient catalyst of Pt. These findings would provide theoretical guidance for the future design of electronic devices based on blueP and exploration of its potential in novel catalysts for hydrogen evolution reaction.

1. Introduction

The great potential promised by two-dimensional (2D) materials has driven the continuous exploration and expansion of the 2D materials family [1]. One new group in the family, being 2D phosphorus allotropes, has recently attracted good attention because of their rich structural diversity and stable existence in different forms [2–5]. Among this group, the black phosphorus (blackP) is the most thermodynamically stable 2D phosphorus allotrope. BlackP exhibits many notable properties, e.g., tunable direct band gap varying from 1.51 eV for monolayer to 0.59 eV for five-layers [6], strong in-plane anisotropy in optical conductivity ranging from 2 to 5 μm [7], thickness-dependent on/off ratio over 10^4 [8] and anisotropic mobility of up to 1,000 $cm^2 V^{-1} s^{-1}$ [9], among others. These appealing characteristics have made blackP a potential candidate material for a broad range of applications, such as field-effect transistors (FETs) [9–11], optoelectronics [7,12], batteries [13,14], solar cells [15], and photocatalysts for hydrogen evolution reaction (HER) [8,16], water splitting [17–20], carbon dioxide reduction [21], and nitrogen fixation [22,23].

Recently, another 2D phosphorus allotrope, i.e., the blue phosphorus (blueP), has been discovered. BlueP was first predicted theoretically [24], and then synthesized successfully either using molecular beam epitaxial growth on Au(1 1 1) by taking blackP as the precursor [25] or quasi-free-standing growth on Au(1 1 1) surface functionalized by tellurium [26]. BlueP exhibits a buckled structure of higher symmetry, which can be obtained via direct transformation from the puckered structure of blackP, aided by specific dislocation of certain constituent P atoms [24]. As a close sibling of blackP, blueP has very similar thermodynamic stability as blackP with the ground-state cohesive energy being only a few meV higher than that of blackP [5,24], and was

* Corresponding authors at: Department of Mining and Materials Engineering, McGill University, Montreal, QC H3A 0C5, Canada (P. Ou).
E-mail addresses: pengfei.ou@mail.mcgill.ca (P. Ou), jun.song2@mcgill.ca (J. Song).

https://doi.org/10.1016/j.apsusc.2022.153450
Received 5 March 2021; Received in revised form 11 April 2022; Accepted 17 April 2022
Available online 20 April 2022

demonstrated by Aierken et al. to be even thermodynamically more stable than blackP at temperatures over 135 K [27]. BlueP also exhibits a thickness-dependent band gap ranging from 2.0 eV for monolayer to 1.2 eV for its bulk [24]. The bandgap range endows blueP a great promise for FETs applications [11,28]. Studies have also been performed to investigate the potential applications of few-layer blueP as channel materials in gas sensors [29,30] or anode materials in Li-ion batteries [13].

On the other front, considering the large surface area to volume ratio, 2D blueP has also been demonstrated as a suitable template for hydrogen (H_2) storage and a material component for HER. For instance, John et al. confirmed the suitability of defective blueP as H_2 storage template, and lithium decoration can lead to higher gravimetric H_2 density [31]. BlueP quantum dots have been predicted to be capable of functioning as a HER catalyst, yielding higher reducing capabilities and better photocatalytic performance as the size increases [32]. The large-area growth of blueP nanosheets on the metal substrate advances significantly owing to the small lattice mismatch, so far, the epitaxial growth of monolayer blueP has been realized on Au(1 1 1) [25,33,34], tellurium monolayer functionalized Au(1 1 1) [26], and Cu_3O_2/Cu(1 1 1) [35] substrates. Several theoretical studies have also examined the interface properties between monolayer blueP and different metal substrates, including Pd(1 1 1), Pd(1 1 0), Pd(1 0 0), Al(1 1 1), Au(1 1 0), and Ni(1 0 0) [31] as well as β-Sn(1 0 0), Au(1 1 1), and Ni(1 1 1) [36]. Naturally, the electronic and chemical properties of synthesized blueP are not expected to be affected by the substrates due to van der Waals interaction. A counterintuition example is that the electron tunneling from the substrate significantly influences the chemical reactions on the surface of the catalysts supported on metals although these reactions occur directly on the catalyst surface instead of the substrates [37]. In this sense, we require a more comprehensive knowledge of substrate coupling on the electronic and chemical properties of monolayer blueP and thus make a substantial contribution to accelerating the development of its applications.

The present study directly targets to examine the substrate coupling on the structural, electronic, and chemical properties of metal-blueP contacts. We systematically investigated the commensurate interfaces between monolayer blueP and several representative transition metal substrates, i.e., Pd, Ir, and Pt, by employing *ab initio* density functional theory (DFT) calculations. These chosen metal surfaces offer minimal lattice mismatch with blueP and cover a considerable range of work functions, which may serve as potential contact materials or growth substrates for blueP. Our results confirmed that a Schottky contact was established in all contacts considered, and the relation between Schottky barrier height (SBH) and metal work function (WF) depicted a picture of partial Fermi level pinning (FLP). It is further illustrated that the incorporation of metal substrates would significantly alter the chemical properties of adsorbed monolayer blueP. The binding strength of hydrogen has been demonstrated to be greatly enhanced by the presence of the metal substrate, owing to the charge transfer from the metal substrate to monolayer blueP to render a stronger H—P coupling as well as a stronger interfacial interaction post hydrogen adsorption. This consequently can render the Gibbs free energy of hydrogen adsorption to a level (e.g., 0.16 eV with blueP on Ir(1 1 1)) comparable to the most efficient transition metal catalyst of Pt for HER.

2. Computational details

Ab initio DFT calculations [38] were performed using the Vienna *ab initio* simulation package (VASP) with the projector augmented-wave (PAW) method [39] and the Ceperley-Alder local density approximation (LDA) [40], with the exchange-correlation functional parameterized by Perdew and Zunger. Fig. 1 illustrates the metal-blueP slab model used in the calculations, consists of a monolayer blueP supported on a metal substrate that contains a slab of 6 atomic layers. A vacuum layer of more than 15 Å in thickness was introduced along the direction perpendicular to the blueP nanosheet to ensure negligible interaction between periodic images. The energy cut-off was set to 400 eV. The metal substrate was taken to conform to the lattice of blueP. The bottommost layer of metal atoms was fixed with respect to their bulk positions, meanwhile, all the other atoms were allowed to relax. The structural relaxation was converged when the force on any given atom fell under 0.01 eV $Å^{-1}$, and the electronic optimization stopped when the total energy difference between the neighboring optimization loop was smaller than 10^{-6} eV. A gamma-centered $6 \times 6 \times 1$ and $8 \times 8 \times 1$ *k*-point meshes were used for structural and electronic optimization, respectively. For the heaviest element, Pt, the spin–orbit coupling effect was examined and confirmed to only have a negligible effect on the energy. The long-range dispersion correction was not included since significant attractive contributions of van der Waals interactions tend to overestimate the binding energy when results were from LDA calculations [41]. The work functions of transition metals were determined from DFT calculations using the equation of $WF_{metal} = E^{vac} - \epsilon_F$, where WF_{metal}, E^{vac}, and ϵ_F denote the work function, vacuum potential, and Fermi energy, respectively.

The computational hydrogen electrode (CHE) model [42] was adopted to establish the free energy profile of HER on metal-blueP systems, in which the Gibbs free energy for a pair of proton and electron $G(H^+ + e^-)$ is equal to half of a hydrogen molecule ($1/2\ G(H_2)$) under standard reaction conditions (i.e., pH $= 0$, $T = 298.15$ K, and $P =$ 1 bar) with zero external potential. The ΔG is then determined by the equation: $\Delta G = \Delta E + \Delta ZPE - T\Delta S$, where ΔE represents the electronic energy difference directly obtained from DFT calculations, ΔZPE for the change in zero-point energy, T for the temperature ($T = 298.15$ K), and ΔS for the entropy change. The contributions of zero-point energies and entropies of the HER species were estimated from the vibrational frequencies, only considered the vibrational modes for adsorbates, and neglected the contributions from metal substrates and blueP. We used the data in the NIST database to calculate the vibrational frequency and entropy of the molecule in its gas phase [43].

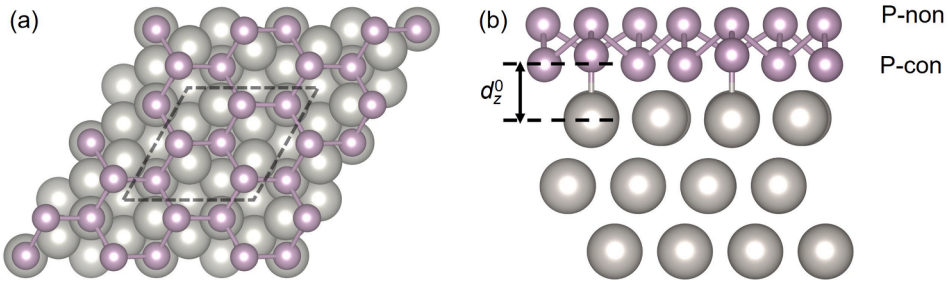

Fig. 1. (a) Top and (b) side perspectives of monolayer blueP adsorbed on the (1 1 1) surface of metal substrates. The black dashed region indicates the unit cell in the calculations. "P-con" and "P-non" indicate P atoms directly and not directly in contact with metal substrates, respectively (purple, phosphorus; grey, Pd, Ir, or Pt). (For interpretation of the references to color in this figure legend, the reader is referred to the web version of this article.)

3. Results and discussion

3.1. Geometry and stability

The optimized planar lattice constant of monolayer blueP is 3.22 Å which is in good agreement with those reported in the previous experimental measurements [25] and theoretical studies [24,29,44]. The metal-blueP contact comprises a monolayer blueP interfacing with three different transition metal substrates exhibiting the (1 1 1) surface (with work functions ranging from 5.69, 5.74, to 5.96 eV for Pd, Ir, and Pt, respectively), which is the favored orientation with the minimum surface energy. These choices were made to minimize the lattice mismatch, i.e., to ensure that a (2 × 2) unit cell of the metal substrate match closely with the ($\sqrt{3} \times \sqrt{3}$)R30° unit cell of blueP (Fig. 1). The maximum and minimum compressive strains between the monolayer blueP and these transition metals are 2.6% and 0.4% for Ir(1 1 1) and Pt(1 1 1), respectively. The metal lattice was taken to conform to that of blueP, to capture details of the electronic behaviors at the examined interface consistently and comparatively. For each metal-blue system, relative in-plane rotations (0°, 60°, and 120°) and alignments (on the top site, in the fcc and hcp hollows) between the metal substrate and blueP were considered to create different initial configurations, from which the most stable geometry (being the one with the highest binding strength post relaxation, see Eq. (1) below) of the metal-blueP contact was thus determined. With the stable metal-blueP systems identified, we found that for all the systems, the metal layer at the contact stays planar, whereas the bottom layer of blueP undergoes substantial distortion. Such distortion in blueP results from a strong interaction between the P and underlying metal atoms.

For quantitative analysis of the metal-blueP contact, we denoted the equilibrium separation distance between the metal substrate and blueP as d_z^0, illustrated in Fig. 1. Consider the bottom layer of blueP is corrugated, we use the average coordinate of atoms in the layer to calculate d_z^0, with the values of d_z^0 summarized in Table 1. Despite different d_z^0 values, we note that the relative in-plane positions between blueP and the underlying substrate stay the same for all systems considered. As depicted in Fig. 1a, the top three P atoms in the supercell sit above the top sites, fcc and hcp hollows; whereas, the bottom three P atoms reside above the triangular centers constructed by top sites, fcc and hcp hollows.

To estimate the structural stability of metal-blueP contacts, the binding strength is evaluated in terms of the binding energy per P atom, which is defined as

$$E_b = (E_{metal} + E_{blueP} - E_{metal-blueP})/n \quad (1)$$

where E_{metal} and E_{blueP} denote the energies of the isolated metal substrate and blueP, $E_{metal-blueP}$ represents the total energy of metal-blueP contact, and n denotes the number of P atoms in direct contact with the metal substrate, respectively. The calculated binding energies are ranging from 0.84 to 1.68 eV. The positive binding energies indicate that the metal-blueP contacts are thermodynamically stable. As shown in Table 1, blueP is found to be chemically adsorbed on the metal surfaces studied herein as the binding energies are larger than 0.5 eV. We note that these *d*-electron metals interact much stronger with blueP compared to blackP and MoS_2 [45–47].

3.2. Electronic properties

The contact nature (e.g., Schottky vs. ohmic and p-type vs. n-type) is one of the key properties that affects the transport behavior and device performance of the metal-semiconductor junction (MSJ). To elucidate the nature of these metal-blueP contacts, the band structures of three different metal-blueP interfaces were calculated and illustrated in Fig. 2, and the formation of Schottky contact is confirmed in all metal-blueP junctions by the deduced band edges of blueP. Strictly speaking, the terminology band is only suitable for homogeneous crystals, whereas, for heterogeneous MSJs with hybridization of orbitals, the CBM and VBM on the semiconductor side can be recognized by neglecting the spilled hybridization states as gap states [46]. As indicated in the projected band structures in Fig. 2, the CBM and VBM of blueP are determined by band edges contributed from the main P *p*-orbitals states (green dots) at K and Γ point, respectively [46–49]. When contacting metal surfaces, the conduction bands of monolayer blueP are preserved well, but the valence bands are severely hybridized with the *d*-orbitals of transition metals. Electron or hole SBH ($\Phi_V^{e/h}$) can be determined from the energy difference between the Fermi energy of MSJ and the CBM or VBM of the contacted blueP, respectively. As shown in Fig. 2, those bands of blueP with small weights crossing the Fermi level is a result of band hybridization at metal-blueP junction. Consequently, the projected main P *p*-orbital states are used to determine the CBM/VBM and bang gap of blueP. The band gap of blueP becomes 1.20, 1.18, and 1.19 eV respectively when contacts with Pd(1 1 1), Ir(1 1 1), and Pt(1 1 1) substrates, substantially smaller than that of free-standing monolayer blueP (1.86 eV). The band gap reduction is due to the energy bands broadening perturbed by the inclusion of metal substrates. Additionally, the extension of blueP states at the band edges to the band gap region induces a metallic character in blueP. Ir(1 1 1)-blueP contact forms an n-type Schottky barrier with electron SBH of 0.66 eV, while in contrast, the contacts of blueP with Ir(1 1 1) and Pt(1 1 1) substrates render p-type Schottky barriers with hole SBHs of 0.46 and 0.57 respectively. Another apparent consequence of adsorbing the blueP directly onto the metal substrate is the Fermi level being pinned within the band gap of blueP, which is ascribed to the high work functions of the chosen metals. To quantitively describe the degree of FLP, we adopted the pinning factor S with the definition of

$$S = d\Phi_V^{e/h} \Big/ \mathrm{dWF}_{metal} \quad (2)$$

where $\Phi_V^{e/h}$ is the vertical SBH in n-type or p-type metal-blueP contacts, and WF_{metal} is the work function of isolated metal substrates. Derived

Table 1
Metrics characterizing structures and energetics for the free-standing blueP and metal-blueP systems. Here, WF_{metal} indicates the work function of metals, ε denotes the lattice mismatch between metal and blueP, d_z^0 and d_z^H are the equilibrium separation distance between metals and blueP without and with H adsorption respectively, d_{H-P} is the length of H—P bond, θ is the angle between the H—P bond and the planar surface of blueP. DIS is defined as the weighted average of displacements of each P atom with respect to its original position in its bulk form. Also listed are the values of conduction band minimum (CBM) and valence band maximum (VBM) of blueP in metal-blueP, the Gibbs free energy of H adsorption (ΔG_{*H}) on the basal plane of a free-standing blueP or metal-blueP system.

	WF_{metal} (eV)	ε (%)	d_z^0 (Å)	d_z^H (Å)	DIS (Å)	CBM* (eV)	VBM* (eV)	ΔG_{*H} (eV)	d_{H-P} (Å)	θ (°)
Pristine blueP								1.07	1.52	43.1
Pd(1 1 1)-blueP	5.69	1.1	1.91	1.72	0.14	0.49	0.50	0.40	1.45	87.4
Ir(1 1 1)-blueP	5.76	2.6	1.80	1.72	0.16	0.67	0.52	0.16	1.46	52.5
Pt(1 1 1)-blueP	5.96	0.4	1.83	1.66	0.15	0.58	0.57	0.39	1.46	54.0

*The band edges of monolayer blueP are −4.46 and −6.32 eV with respect to the vacuum level, and the CBM/VBM of metal-blueP junctions are determined by projecting the main P *p*-orbital states and treating the minor P *p*-orbital states as gap states.

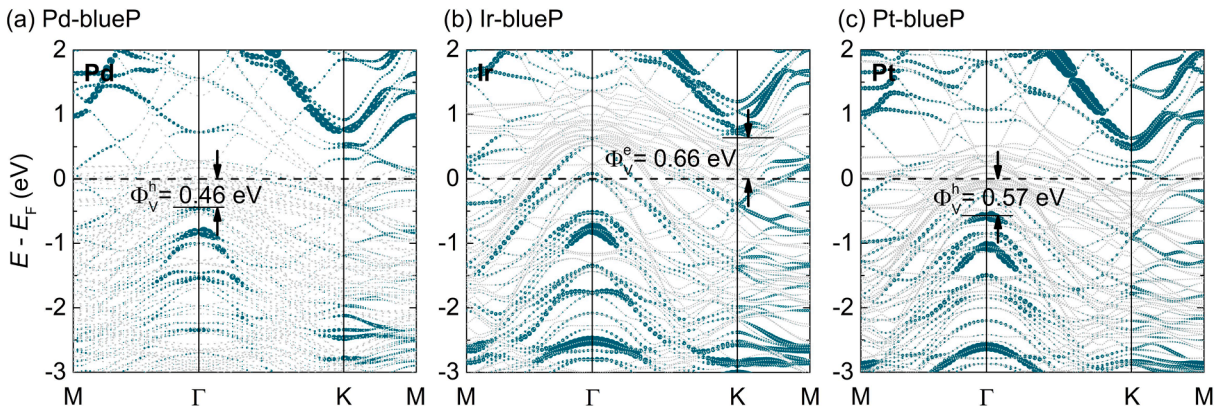

Fig. 2. Band structures of monolayer blueP adsorbed on (a) Pd(1 1 1), (b) Ir(1 1 1), and (c) Pt(1 1 1) surfaces, respectively. The Fermi level is adjusted to 0 eV and is marked by the black dashed lines in these figures. The green dots indicate the *p*-orbitals projection of monolayer blueP, and the black numbers denote the values of vertical SBHs. (For interpretation of the references to color in this figure legend, the reader is referred to the web version of this article.)

from the Schottky-Mote rule, S varies from $S = 1$ for an unpinned Fermi level and $S = 0$ for a completely pinned Fermi level [48,50]. Realistically, S is usually small for MSJs due to a strong FLP effect. As shown in Fig. 3, for monolayer blueP, the calculated pinning factor is about $S = 0.35$ for hole SBH and 0.37 for electron SBH, which is slightly higher than the calculated values of $S = 0.28$ for monolayer blackP [51] and $S = 0.27$ for monolayer MoS_2 [49,52], and even higher than the experimental measurements for monolayer MoS_2 [53]. This pinning factor indicates that the metal-blueP interface would be strongly impacted by the FLP effect.

The afore-mentioned band hybridization and FLP possibly result from factors such as charge transfer and overlap of atomic orbitals between the metal substrates and blueP. We first analyzed the charge density difference (CDD, $\Delta\rho$) to visualize the charge redistribution at the interface,

$$\Delta\rho = \rho_{\text{metal-blueP}} - \rho_{\text{metal}} - \rho_{\text{blueP}} \tag{3}$$

where $\rho_{\text{metal-blueP}}$, ρ_{metal}, and ρ_{blueP} denote the plane-averaged charge densities of the metal-blueP interfaces, isolated metal substrates, and monolayer blueP, respectively. Fig. 4 depicts the spatial variation of $\Delta\rho$ along the vertical direction perpendicular to the interface. Zooming in to the characteristics near the interface, we see an obvious charge redistribution between the two topmost layers of metals and the bottom layer of blueP. Compared with other metal-2D materials contacts, e.g., graphene, the major difference that distinguishes metal-blueP contact from metal-graphene one [54] is the existence of a charge accumulation area (green shaded area), which agrees well with the fact that blueP is more chemically reactive than graphene. On the other hand, if we further include other contacts, such as metal-graphene [54] and metal-MoS_2 [45,46] in the literature as well as metal-blueP contacts in the present study in the pool for comparison, we note that in all cases, both of these contacts share the common feature of a charge depletion region (blue shaded area). In general, both charge accumulation and depletion contribute to the interfacial charge redistribution, which results in a polarization of electron wave functions, i.e., the formation of interface electric dipole. Therefore, the interface band alignment is modified by the interface electric dipole formation [55]. Meanwhile, examining the charge redistribution for all metal-blueP interfaces (Fig. 4a-c) considered, we note that the overall magnitude of charge redistribution is correlated to the separation distance d_z^0. For instance, we see that the Ir (1 1 1)-blueP interface, with the smallest d_z^0, exhibits the most significant charge redistribution. To further confirm such correlation with the separation distance, we took the Pd(1 1 1)-blueP interface as a representative and manually adjusted the separation distance. We found out that, charge redistribution is much reduced to an order of magnitude smaller at Pd(1 1 1)-blueP interface when the separation distance increases to 4.5 Å (Fig. 4d), compared to that of equilibrium distance. The increased separation distance weakens the interface interaction and decreases the interface electric dipole between metals and blueP, therefore reducing the FLP at metal-blueP interfaces.

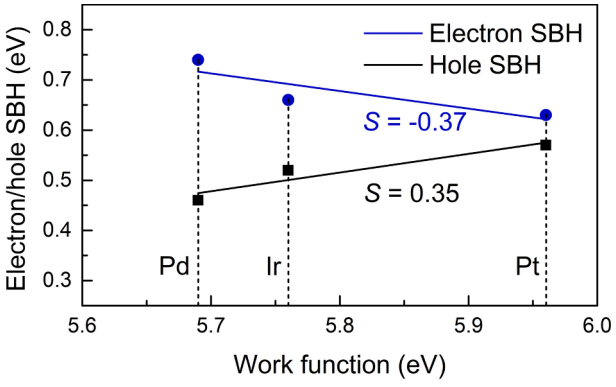

Fig. 3. Variation in Schottky barrier heights of monolayer blueP versus the work functions of Pd(1 1 1), Ir(1 1 1), and Pt(1 1 1), S is the pinning factor derived from the Schottky-Mote rule.

To assess the interface behavior from the orbital-wise perspectives, we further substantiated the strong metal-blueP hybridization at the interface region by analyzing the partial density of states (PDOS), as illustrated in Fig. 5. A direct hybridization of orbitals is observed at the interface region of metal-blueP contact. The separation distances in the vertical direction between bottom P atoms in blueP and the metal atoms on the surface (1.80–1.91 Å) are much smaller than that of van der Waals separation (for instance, 3.34 Å in graphite), which maximize the spatial overlapping at the interface region. Besides, the lone pairs of P atoms also constitute a strong interaction between blueP and metals. According to the Valence Shell Electron Pair Repulsion Theory (VSEPR), each P atom in blueP forms valence bonds with three nearest neighbors, therefore each P atom possesses a lone pair that is not shared with other P atoms. The lone pairs exhibit relatively high chemical reactivity and tend to react with the metal atoms on the surface, rendering a stronger interaction between the blueP and metals. Furthermore, a detailed analysis of PDOS discloses that the gap states are dominated by the *d*-orbitals character of metals and primarily contribute to the lower part of the band gap when blueP contacts with Pd and Pt, compared to the upper part when contact with Ir.

Generally, the modification of metal WFs can be weakened by increasing separation between metal contacts and blueP, meanwhile, the interface hybridization is mitigated, which results in fewer gap states and therefore Fermi level unpinning. To quantitatively analyze the CBM

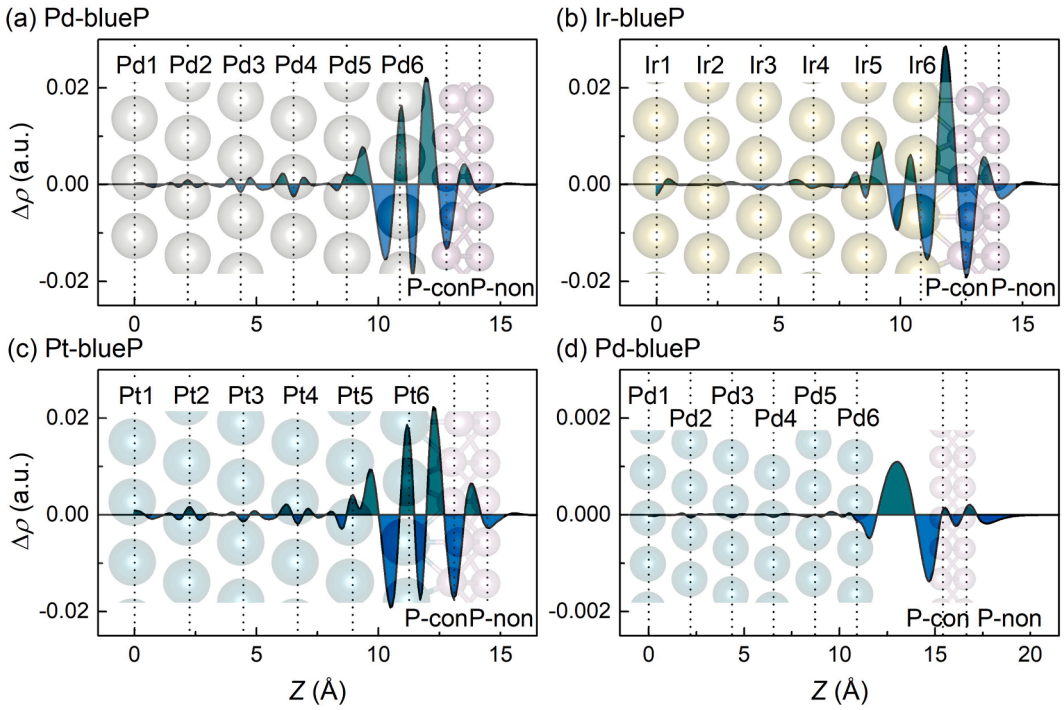

Fig. 4. Plane-averaged charge density difference along the vertical direction perpendicular to the (a) Pd(1 1 1)-blueP, (b) Ir(1 1 1)-blueP, and (c) Pt(1 1 1)-blueP interfaces at the equilibrium distance, as well as (d) Pd(1 1 1)-blueP system at a distance of 4.5 Å. Green and blue colored regions indicate the charge accumulation and depletion regions, respectively. Note that the *Z*-axis starts (i.e., $Z = 0$) from the bottom metal layer, and increases towards the interface, so is the metal layer numbering (c.f. Fig. 1). (For interpretation of the references to color in this figure legend, the reader is referred to the web version of this article.)

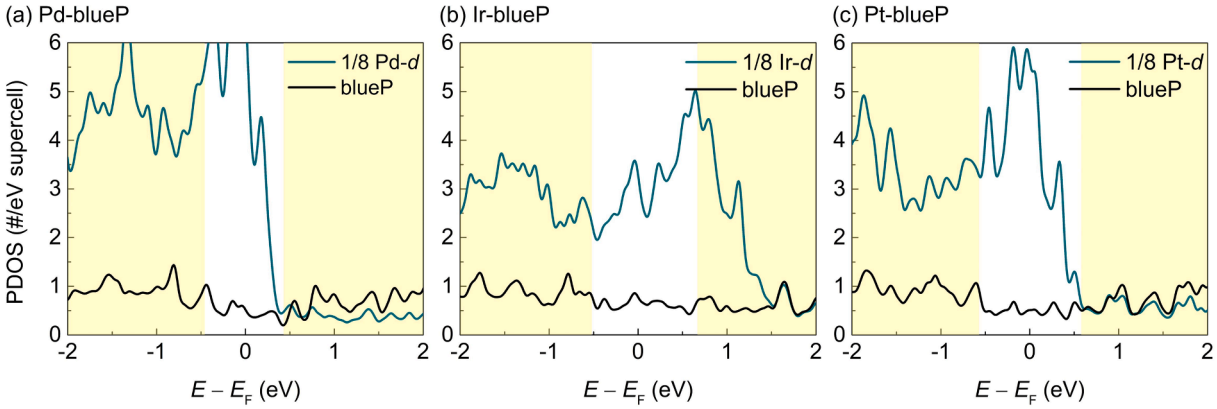

Fig. 5. PDOSs of blueP (black line) and metal (green line) in the metal-blueP contacts for (a) Pd(1 1 1), (b) Ir(1 1 1), and (c) Pt(1 1 1), respectively. Yellow-colored areas represent the band edges of the conduction band and valence band, derived by the projected main P *p*-orbital states in the band structures, as shown in Fig. 2. "1/8 Pd-*d*" in (a), for example, means that the PDOS of *d*-orbital for Pd atoms is reduced to 1/8 for a better comparison with PDOS of blueP. (For interpretation of the references to color in this figure legend, the reader is referred to the web version of this article.)

and VBM of blueP in the metal-blueP contacts, their exact locations are determined by the Schottky-Mott rule as follows:

$$\mathrm{VBM_{ideal}} = -\left(E_g/2 - (\mathrm{WF_{metal}} - \mathrm{WF_{blueP}})\right) \quad (4)$$

$$\mathrm{CBM_{ideal}} = E_g + \mathrm{VBM_{ideal}} \quad (5)$$

where E_g, $\mathrm{WF_{metal}}$, and $\mathrm{WF_{blueP}}$ represent the band gap of monolayer blueP, the WFs of isolated metals, and of isolated blueP, respectively. As shown in Fig. 6(a)-(c), green and blue bars depict the dependence of CBM and VBM as a function of interfacial separation distance together with the black numbers indicating their exact locations, and the orange dashed lines and numbers indicating the ideal locations of VBM and CBM calculated from Eqs. (4) and (5). At an interface separation of 6.0 Å, the exact locations of CBM and VBM for all metal-blueP contacts almost match the ideal locations predicted from the Schottky-Mott rule, which reflects that SBHs are exclusively determined by the WF difference between isolated metals and blueP. Therefore, the insertion of a buffer layer (e.g., graphene and MoS_2) between metals and blueP is suggested to be a promising approach for the FL unpinning.

3.3. Chemical properties

Aside from the modifications to the electronic properties, the strong interaction between the monolayer blueP and metal substrate is also expected to alter the chemical properties of monolayer blueP. A fundamentally significant and technologically important electrochemical reaction, HER, has been selected as an example to exploit the

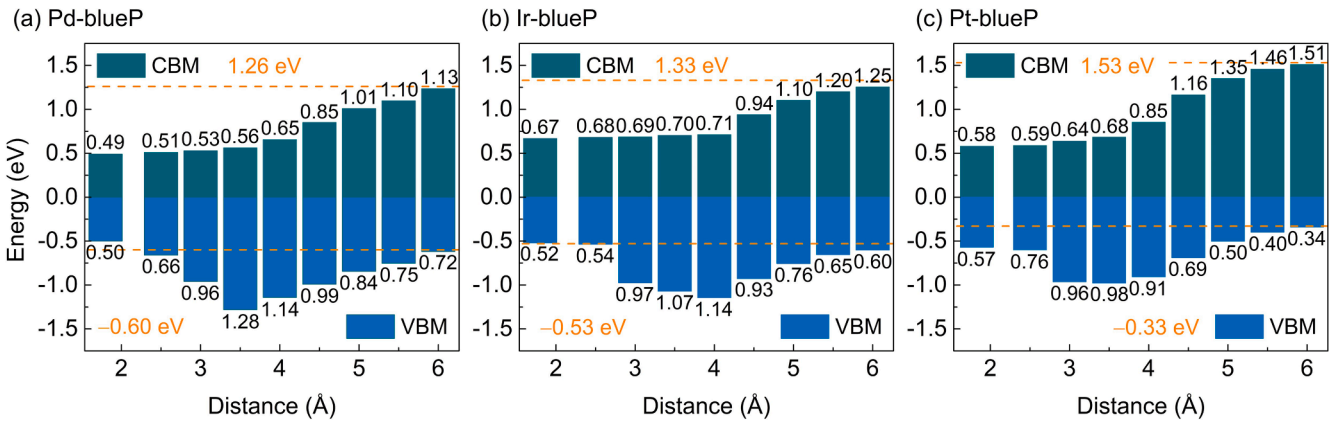

Fig. 6. Exact locations of CBM and VBM of monolayer blueP with respect to the interface distance in (a) Pd-blueP, (b) Ir-blueP, and (c) Pt-blueP contacts, respectively. The leftmost color bar indicates the values at equilibrium separation distance, and the horizontal orange dashed line corresponds to the ideal locations of CBM and VBM determined from the conventional Schottky-Mott rule. (For interpretation of the references to color in this figure legend, the reader is referred to the web version of this article.)

potential of tuning the chemical reactivity on the surface of blueP through metal substrate coupling.

First, the most stable geometries of H adsorption on pristine monolayer blueP and overlayer on the metal substrates are determined by examining all the possible initial configurations with symmetry considerations. As shown in Fig. 7, the upper row illustrates the top and side views of the most stable geometries when one H is adsorbed on the surfaces. According to the Sabatier principle [56], the free energy change when one H adsorbed on the surface (ΔG_{*H}) should be near zero to achieve the maximum reaction rate. As shown in Table 1, the calculated ΔG_{*H} are 0.40, 0.16, and 0.39 eV for blueP on Pd(1 1 1), Ir(1 1 1), and Pt(1 1 1) substrates respectively, compared to the value of 1.07 eV on pristine monolayer blueP. We note that the ΔG_{*H} of Ir(1 1 1)-blueP is as low as the value of Pt (~0.1 eV) [57]. In addition to the Gibbs free energy of H adsorption, the geometrical variations are also observed between the considered systems, as measured by the angle (θ) between the H—P bond and the planar surface of blueP. We can see in Table 1 and Fig. 7, θ are 52.5° and 54.0° for Ir(1 1 1)-blueP and Pt(1 1 1)-blueP systems, respectively, which are not far away from the 43.1° on a free-standing blueP. In stark contrast, the H atom prefers to adsorb on the top of P atoms in the Pd(1 1 1)-blueP system with a θ of 87.4°. These results collectively reflect that either the Gibbs free energy or the geometry of H adsorption can be adjusted with a proper choice of the metal electrode. Such a tunability would remarkably affect the HER efficiency on the basal plane of adsorbed blueP.

Furthermore, to further unravel the inner reason of enhanced H adsorption due to the substrate coupling, the CDD between H and the pristine blueP and metal-blueP surfaces were calculated by $\Delta\rho = \rho_{H/metal-blueP} - \rho_H - \rho_{metal-blueP}$, similar to eqn. (3). As shown in Fig. 7, the lower row demonstrates the side views of the contour images of CDD. Obviously, more charge participates in the formation of H—P covalent bonds on Pd(1 1 1), Ir(1 1 1), and Pt(1 1 1) substrates, which is consistent with the enhanced adsorption energy and shortened bond lengths, as shown in Table 1. Apart from the charge redistribution between the blueP and adsorbed H atom, the coupling effect between blueP and metal substrates on the H adsorption was also examined. The parameter of d_z^H is thus introduced to quantify such an effect, which is defined as the average separation between the lower layer of blueP and the topmost layer of metal substrates. With the presence of H, d_z^H is reduced by 0.19, 0.08, and 0.16 Å for Pd, Ir, and Pt respectively, compared to the original value of separation without H adsorption. Overall, the enhanced H adsorption originates from two aspects:[45] (a) the stronger metal-blueP hybridization at the interface region (Fig. 4) induce more charges transferred from metal substrates to blueP in the formation of a stronger H—P covalent bonding; (2) the adsorbed H atom is acting as a "nail" to fasten the metal substrates and blueP together, and thus results in a

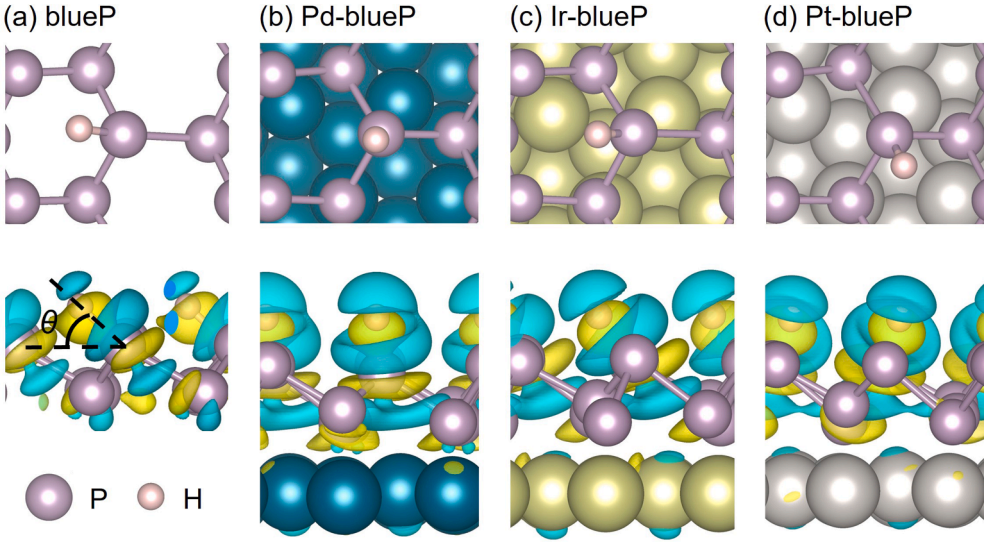

Fig. 7. Top views of the most stable geometries (upper row) and side views of the contour images of charge density difference (lower row) when one H atom adsorbed on (a) a free-standing blueP, (b) Pd(1 1 1)-blueP, (c) Ir(1 1 1)-blueP, and (d) Pt(1 1 1)-blueP systems, respectively. θ refers to the angle between the H—P bond and the planar surface of blueP. The yellow and blue colors indicate the charge accumulation and depletion, respectively. The *iso*-surface value of the contour plot is set to 0.002 e Bohr^{-3}. (For interpretation of the references to color in this figure legend, the reader is referred to the web version of this article.)

strong metal-blueP interface.

4. Conclusions

To summarize, systematic *ab initio* DFT calculations were performed on contacts between monolayer blueP and three representative transition metal substrates of Pd, Ir, and Pt, and the implications of metal-blueP coupling to their electronic and chemical properties. Our results showed that the metal-blueP contacts are thermodynamically stable, and the strong interaction between metals and blueP led to substantial corrugation in the bottom layer of blueP. On the front of electronic properties, the Schottky barrier contacts were formed for each metal substrate, and the relation between SBHs and metal work functions depicted a picture of partial Fermi-level pinning. The calculated CBM and VBM at metal-blueP interfaces severely deviate from the predictions from the Schottky-Motte rule, due to a notable band realignment ascribed to the interface dipole formation. Besides, the interface dipole formation also results in a remarkable interface charge redistribution since the adsorbed blueP would significantly modify the metal work functions. Meanwhile, on the front of chemical properties, the metal-blueP coupling was confirmed to have a substantial effect on tuning the free energy of H adsorption on blueP overlayer. By examining the charge density redistribution, we found that the enhanced H adsorption originates from two aspects, one being more charge involved in the bond formation which gives a stronger H—P covalent bond, the other being the adsorbed H atom acting as a "nail" to pin the metals and blueP which results in a strong metal-blueP interface. These instrumental findings might guide the future design of electronic and optoelectronic devices based on this promising 2D nanomaterial and exploit its potential in catalyzing the hydrogen evolution reaction and related overall water splitting.

CRediT authorship contribution statement

Pengfei Ou: Conceptualization, Methodology, Software, Formal analysis, Writing – original draft. **Guoqiang Lan:** Software, Writing – review & editing. **Yiqing Chen:** Software, Validation. **Xiao-Yan Li:** Software, Writing – review & editing. **Xiao Zhou:** Software, Writing – review & editing. **Cheng Chen:** Software, Validation. **Fanchao Meng:** Software, Validation. **Jun Song:** Conceptualization, Writing – review & editing, Supervision.

Declaration of Competing Interest

The authors declare that they have no known competing financial interests or personal relationships that could have appeared to influence the work reported in this paper.

Acknowledgements

This research is supported by the NSERC Discovery grant (grant # RGPIN-2017-05187), New Frontiers in Research Fund - Exploration (grant # NFRFE-2019-00533), and McGill Engineering Doctoral Award (MEDA). F. M. acknowledges financial support from National Natural Science Foundation of Guangdong Province-General Program, China (No. 2020A1515011069). We also would like to acknowledge Compute Canada for providing computing resources.

References

[1] A.J. Mannix, B. Kiraly, M.C. Hersam, N.P. Guisinger, Synthesis and chemistry of elemental 2D materials, Nat. Rev. Chem. 1 (2017) 1–14.
[2] F. Bachhuber, J. vonAppen, R. Dronskowski, P. Schmidt, T. Nilges, A. Pfitzner, R. Weihrich, The extended stability range of phosphorus allotropes, Angew. Chem. Int. Ed. 53 (43) (2014) 11629–11633.
[3] M. Wu, H. Fu, L. Zhou, K. Yao, X.C. Zeng, Nine new phosphorene polymorphs with non-honeycomb structures: a much extended family, Nano Lett. 15 (5) (2015) 3557–3562.
[4] J. Liu, Y. Guo, S. Zhang, Q. Wang, Y. Kawazoe, P. Jena, New phosphorene allotropes containing ridges with 2-and 4-coordination, J. Phys. Chem. C 119 (43) (2015) 24674–24680.
[5] J. Guan, Z. Zhu, D. Tománek, Phase Coexistence and Metal-Insulator Transition in Few-Layer Phosphorene: A Computational Study, Phys. Rev. Lett. 113 (2014), 046804.
[6] J. Qiao, X. Kong, Z.-X. Hu, F. Yang, W. Ji, High-mobility transport anisotropy and linear dichroism in few-layer black phosphorus, Nat. Commun. 5 (2014) 4475.
[7] F. Xia, H. Wang, Y. Jia, Rediscovering black phosphorus as an anisotropic layered material for optoelectronics and electronics, Nat. Commun. 5 (2014) 4458.
[8] H. Liu, A.T. Neal, Z. Zhu, Z. Luo, X. Xu, D. Tománek, P.D. Ye, Phosphorene: an unexplored 2D semiconductor with a high hole mobility, ACS Nano 8 (2014) 4033–4041.
[9] L. Li, Y. Yu, G.J. Ye, Q. Ge, X. Ou, H. Wu, D. Feng, X.H. Chen, Y. Zhang, Black phosphorus field-effect transistors, Nat. Nanotechnol. 9 (2014) 372.
[10] M. Buscema, D.J. Groenendijk, S.I. Blanter, G.A. Steele, H.S. Van Der Zant, A. Castellanos-Gomez, Fast and broadband photoresponse of few-layer black phosphorus field-effect transistors, Nano Lett. 14 (2014) 3347–3352.
[11] L. Banerjee, A. Mukhopadhyay, A. Sengupta, H. Rahaman, Performance analysis of uniaxially strained monolayer black phosphorus and blue phosphorus n-MOSFET and p-MOSFET, J. Comput. Electron. 15 (2016) 919–930.
[12] J. Xie, M. Si, D. Yang, Z. Zhang, D. Xue, A theoretical study of blue phosphorene nanoribbons based on first-principles calculations, J. Appl. Phys. 116 (2014), 073704.
[13] Q.-F. Li, C.-G. Duan, X. Wan, J.-L. Kuo, Theoretical prediction of anode materials in Li-ion batteries on layered black and blue phosphorus, J. Phys. Chem. C 119 (2015) 8662–8670.
[14] X. Xiao, M. Wang, J. Tu, S. Jiao, The potential application of black and blue phosphorene as cathode materials in rechargeable aluminum batteries: a first-principles study, Phys. Chem. Chem. Phys. 21 (13) (2019) 7021–7028.
[15] Y. Yang, J. Gao, Z. Zhang, S. Xiao, H.H. Xie, Z.B. Sun, J.H. Wang, C.H. Zhou, Y. W. Wang, X.Y. Guo, Black Phosphorus Based Photocathodes in Wideband Bifacial Dye-Sensitized Solar Cells, Adv. Mater. 28 (2016) 8937–8944.
[16] X. Zhu, T. Zhang, Z. Sun, H. Chen, J. Guan, X. Chen, H. Ji, P. Du, S. Yang, Black Phosphorus Revisited: A Missing Metal-Free Elemental Photocatalyst for Visible Light Hydrogen Evolution, Adv. Mater. 29 (17) (2017) 1605776.
[17] W. Lei, Y. Mi, R. Feng, P. Liu, S. Hu, J. Yu, X. Liu, J.A. Rodriguez, J.-o. Wang, L. Zheng, K. Tang, S. Zhu, G. Liu, M. Liu, Hybrid 0D–2D black phosphorus quantum dots–graphitic carbon nitride nanosheets for efficient hydrogen evolution, Nano Energy 50 (2018) 552–561.
[18] M. Zhu, Z. Sun, M. Fujitsuka, T. Majima, Z-Scheme Photocatalytic Water Splitting on a 2D Heterostructure of Black Phosphorus/Bismuth Vanadate Using Visible Light, Angew. Chem. Int. Ed. 57 (8) (2018) 2160–2164.
[19] X.u. Gao, Y. Shen, Y. Ma, S. Wu, Z. Zhou, A water splitting photocatalysis: Blue phosphorus/g-GeC van der Waals heterostructure, Appl. Phys. Lett. 114 (9) (2019) 093902.
[20] K. Ren, S. Wang, Y.i. Luo, Y. Xu, M. Sun, J. Yu, W. Tang, Strain-enhanced properties of van der Waals heterostructure based on blue phosphorus and g-GaN as a visible-light-driven photocatalyst for water splitting, RSC Adv. 9 (9) (2019) 4816–4823.
[21] C. Han, J. Li, Z. Ma, H. Xie, G.I. Waterhouse, L. Ye, T. Zhang, Black phosphorus quantum dot/gC_3N_4 composites for enhanced CO_2 photoreduction to CO, Sci. China Mater. 61 (2018) 1159–1166.
[22] L. Zhang, L.X. Ding, G.F. Chen, X. Yang, H. Wang, Ammonia Synthesis Under Ambient Conditions: Selective Electroreduction of Dinitrogen to Ammonia on Black Phosphorus Nanosheets, Angew. Chem. 131 (2019) 2638–2642.
[23] P. Qiu, C. Xu, N. Zhou, H. Chen, F. Jiang, Metal-free black phosphorus nanosheets-decorated graphitic carbon nitride nanosheets with C–P bonds for excellent photocatalytic nitrogen fixation, Appl. Catal. B 221 (2018) 27–35.
[24] Z. Zhu, D. Tománek, Semiconducting layered blue phosphorus: a computational study, Phys. Rev. Lett. 112 (2014), 176802.
[25] J.L. Zhang, S. Zhao, C. Han, Z. Wang, S. Zhong, S. Sun, R. Guo, X. Zhou, C.D. Gu, K. D. Yuan, Z. Li, W. Chen, Epitaxial Growth of Single Layer Blue Phosphorus: A New Phase of Two-Dimensional Phosphorus, Nano Lett. 16 (2016) 4903–4908.
[26] C. Gu, S. Zhao, J.L. Zhang, S. Sun, K. Yuan, Z. Hu, C. Han, Z. Ma, L.i. Wang, F. Huo, W. Huang, Z. Li, W. Chen, Growth of Quasi-Free-Standing Single-Layer Blue Phosphorus on Tellurium Monolayer Functionalized Au(111), ACS Nano 11 (5) (2017) 4943–4949.
[27] Y. Aierken, D. Çakır, C. Sevik, F.M. Peeters, Thermal properties of black and blue phosphorenes from a first-principles quasiharmonic approach, Phys. Rev. B 92 (2015), 081408.
[28] E. Montes, U. Schwingenschlögl, High-Performance Field-Effect Transistors Based on αP and βP, Adv. Mater. 31 (18) (2019) 1807810.
[29] N. Liu, S.i. Zhou, Gas adsorption on monolayer blue phosphorus: implications for environmental stability and gas sensors, Nanotechnology 28 (17) (2017) 175708.
[30] E. Montes, U. Schwingenschlögl, Superior selectivity and sensitivity of blue phosphorus nanotubes in gas sensing applications, J. Mater. Chem. C 5 (22) (2017) 5365–5371.
[31] A. Maity, R. Pinčák, Density functional study of blue phosphorene–metal interface, Eur. Phys. J. B 94 (2021) 77.
[32] S. Zhou, N. Liu, J. Zhao, Phosphorus quantum dots as visible-light photocatalyst for water splitting, Comput. Mater. Sci. 130 (2017) 56–63.

[33] W. Zhang, H. Enriquez, Y. Tong, A. Bendounan, A. Kara, A.P. Seitsonen, A. J. Mayne, G. Dujardin, H. Oughaddou, Epitaxial Synthesis of Blue Phosphorene, Small 14 (2018) 1804066.
[34] C. Grazianetti, G. Faraone, C. Martella, E. Bonera, A. Molle, Embedding epitaxial (blue) phosphorene in between device-compatible functional layers, Nanoscale 11 (2019) 18232–18237.
[35] D. Zhou, Q. Meng, N. Si, X. Zhou, S. Zhai, Q. Tang, Q. Ji, M. Zhou, T. Niu, H. Fuchs, Epitaxial Growth of Flat, Metallic Monolayer Phosphorene on Metal Oxide, ACS Nano 14 (2020) 2385–2394.
[36] L. Qiu, J.C. Dong, F. Ding, Selective growth of two-dimensional phosphorene on catalyst surface, Nanoscale 10 (5) (2018) 2255–2259.
[37] H.-J. Freund, G. Pacchioni, Oxide ultra-thin films on metals: new materials for the design of supported metal catalysts, Chem. Soc. Rev. 37 (2008) 2224–2242.
[38] G. Kresse, J. Furthmüller, Efficiency of ab-initio total energy calculations for metals and semiconductors using a plane-wave basis set, Comput. Mater. Sci. 6 (1) (1996) 15–50.
[39] P.E. Blöchl, Projector augmented-wave method, Phys. Rev. B 50 (24) (1994) 17953–17979.
[40] D.M. Ceperley, B.J. Alder, Ground state of the electron gas by a stochastic method, Phys. Rev. Lett. 45 (7) (1980) 566–569.
[41] Y.i. Gao, X.C. Zeng, Ab initio study of hydrogen adsorption on benzenoid linkers in metal–organic framework materials, J. Phys.: Condens. Matter 19 (38) (2007) 386220.
[42] J.K. Nørskov, J. Rossmeisl, A. Logadottir, L. Lindqvist, J.R. Kitchin, T. Bligaard, H. Jonsson, Origin of the overpotential for oxygen reduction at a fuel-cell cathode, J. Phys. Chem. B 108 (2004) 17886–17892.
[43] C. Ling, X. Bai, Y. Ouyang, A. Du, J. Wang, Single Molybdenum Atom Anchored on N-Doped Carbon as a Promising Electrocatalyst for Nitrogen Reduction into Ammonia at Ambient Conditions, J. Phys. Chem. C 122 (2018) 16842–16847.
[44] L. Huang, B. Li, M. Zhong, Z. Wei, J. Li, Tunable Schottky Barrier at $MoSe_2$/Metal Interfaces with a Buffer Layer, J. Phys. Chem. C 121 (2017) 9305–9311.
[45] W. Chen, E.J.G. Santos, W. Zhu, E. Kaxiras, Z. Zhang, Tuning the Electronic and Chemical Properties of Monolayer MoS_2 Adsorbed on Transition Metal Substrates, Nano Lett. 13 (2013) 509–514.
[46] C. Gong, L. Colombo, R.M. Wallace, K. Cho, The Unusual Mechanism of Partial Fermi Level Pinning at Metal–MoS_2 Interfaces, Nano Lett. 14 (2014) 1714–1720.
[47] Y. Pan, S. Li, M. Ye, R. Quhe, Z. Song, Y. Wang, J. Zheng, F. Pan, W. Guo, J. Yang, J. Lu, Interfacial Properties of Monolayer $MoSe_2$–Metal Contacts, J. Phys. Chem. C 120 (2016) 13063–13070.
[48] C. Kim, I. Moon, D. Lee, M.S. Choi, F. Ahmed, S. Nam, Y. Cho, H.-J. Shin, S. Park, W.J. Yoo, Fermi Level Pinning at Electrical Metal Contacts of Monolayer Molybdenum Dichalcogenides, ACS Nano 11 (2017) 1588–1596.
[49] H. Zhong, R. Quhe, Y. Wang, Z. Ni, M. Ye, Z. Song, Y. Pan, J. Yang, L. Yang, M. Lei, Interfacial properties of monolayer and bilayer MoS_2 contacts with metals: beyond the energy band calculations, Sci. Rep. 6 (2016) 21786.
[50] Y. Liu, P. Stradins, S.-H. Wei, Van der Waals metal-semiconductor junction: Weak Fermi level pinning enables effective tuning of Schottky barrier, Sci. Adv. 2 (2016).
[51] Y. Pan, Y. Wang, M. Ye, R. Quhe, H. Zhong, Z. Song, X. Peng, D. Yu, J. Yang, J. Shi, J. Lu, Monolayer Phosphorene-Metal Contacts, Chem. Mater. 28 (7) (2016) 2100–2109.
[52] Y. Guo, D. Liu, J. Robertson, 3D behavior of Schottky barriers of 2D transition-metal dichalcogenides, ACS Appl. Mater. Interfaces 7 (46) (2015) 25709–25715.
[53] S. Das, H.-Y. Chen, A.V. Penumatcha, J. Appenzeller, High performance multilayer MoS_2 transistors with scandium contacts, Nano Lett. 13 (1) (2013) 100–105.
[54] C. Gong, G. Lee, B. Shan, E.M. Vogel, R.M. Wallace, K. Cho, First-principles study of metal–graphene interfaces, J. Appl. Phys. 108 (12) (2010) 123711.
[55] R.T. Tung, Formation of an electric dipole at metal-semiconductor interfaces, Phys. Rev. B 64 (2001), 205310.
[56] G. Rothenberg, Catalysis: concepts and green applications, Wiley-VCH, 2008, pp. 65.
[57] T. Chao, X. Luo, W. Chen, B. Jiang, J. Ge, Y. Lin, G. Wu, X. Wang, Y. Hu, Z. Zhuang, Atomically dispersed copper–platinum dual sites alloyed with palladium nanorings catalyze the hydrogen evolution reaction, Angew. Chem. Int. Ed. 56 (2017) 16047–16051.